

# Simulations of Frustrated Ising Hamiltonians using Quantum Approximate Optimization

Phillip C. Lotshaw,<sup>1,\*</sup> Hanjing Xu,<sup>2</sup> Bilal Khalid,<sup>2,3</sup> Gilles Buchs,<sup>4,3</sup> Travis S. Humble,<sup>4,3</sup> and Arnab Banerjee<sup>2,3</sup>

<sup>1</sup>*Quantum Information Sciences Section, Oak Ridge National Laboratory, Oak Ridge, TN 37831, USA*

<sup>2</sup>*Purdue Quantum Science and Engineering Institute,  
Purdue University, West Lafayette, IN 47907, USA*

<sup>3</sup>*Quantum Science Center, Oak Ridge National Laboratory, Oak Ridge, TN 37830, USA*

<sup>4</sup>*Quantum Information Sciences Section, Oak Ridge National Laboratory, Oak Ridge, TN 37831, USA*

Novel magnetic materials are important for future technological advances. Theoretical and numerical calculations of ground state properties are essential in understanding these materials, however, computational complexity limits conventional methods for studying these states. Here we investigate an alternative approach to preparing materials ground states using the quantum approximate optimization algorithm (QAOA) on near-term quantum computers. We study Ising spin models on unit cells of square, Shastry-Sutherland, and triangular lattices, with varying field amplitudes and couplings in the material Hamiltonian. We find relationships between the theoretical QAOA success probability and the structure of the ground state, indicating that only a modest number of measurements ( $\lesssim 100$ ) are needed to find the ground state of our nine-spin Hamiltonians, even for parameters leading to frustrated magnetism. We further demonstrate the approach in calculations on a trapped-ion quantum computer and succeed in recovering each ground state of the Shastry-Sutherland unit cell with probabilities close to ideal theoretical values. The results demonstrate the viability of QAOA for materials ground state preparation in the frustrated Ising limit, giving important first steps towards larger sizes and more complex Hamiltonians where quantum computational advantage may prove essential in developing a systematic understanding of novel materials.

## I. INTRODUCTION

Quantum magnetism has been a major focus in condensed matter research ever since the ideas about quantum mechanics were first voiced. The research in this field is motivated by new, disruptive applications in the field of quantum information technology and quantum spintronics, promising extensive impact on future society when addressing grand challenges such as fault-tolerant quantum computing, topologically protected quantum memories, quantum sensors and devices required for cancer treatment, catalysis and sustainable energy [1, 2]. Along with technological advances, quantum magnetism may also provide insights to conceptual elements in quantum physics that we do not fully understand: What is quantum mechanical superposition and entanglement? How does high- $T_c$  superconductivity work? How to fully grasp the concept of time and time-reversal symmetry?

Frustrated quantum magnets serve as ideal testing grounds for many-body quantum physics and quantum phase transitions as  $T \rightarrow 0$ , where quantum fluctuations dominate any other classical or thermal mechanisms [3–7]. Development in this field requires a close synergy between theory and experiment, where calculating the ground state and dispersions of a quantum magnet is paramount to deciphering experimental data for future devices and applications. The smallest building block of a frustrated magnetic Hamiltonian is an antiferromagnetic triangular motif of three spin-1/2's where all the bonds cannot be satisfied simultaneously. In these materials, exchange interactions compete such that it is impossible to satisfy them all simultaneously, see Fig. 1. If all spin configurations are equally favorable, we obtain non-ordered states such as spin liquids [8] or spin glasses [9], or plaquette states [10], each with distinct signatures. In materials exhibiting frustrated magnetism, a range of compromising configurations may be close in energy and the system can be tuned from one state to another by using an external parameter such as chemical doping, pressure or magnetic field [8, 11–14].

Exact solutions of quantum ground states are rare, requiring the field to resort to approximations, assumptions and using semi-classical limits [7, 8, 15, 16]. Classical computational techniques such as the density matrix renormalization group (DMRG) and the quantum Monte-Carlo (QMC) algorithm have limited applicability for systems exhibiting these quantum phases. DMRG is of limited efficacy for long-range entanglement in more than one dimension, which is

---

\* lotshawpc@ornl.gov;

This manuscript has been authored by UT-Battelle, LLC under Contract No. DE-AC05-00OR22725 with the U.S. Department of Energy. The United States Government retains and the publisher, by accepting the article for publication, acknowledges that the United States Government retains a non-exclusive, paid-up, irrevocable, world-wide license to publish or reproduce the published form of this manuscript, or allow others to do so, for United States Government purposes. The Department of Energy will provide public access to these results of federally sponsored research in accordance with the DOE Public Access Plan. (<http://energy.gov/downloads/doe-public-access-plan>)

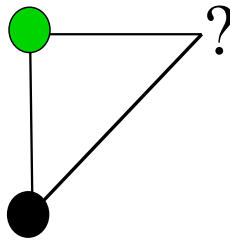


FIG. 1: Example of frustration on an antiferromagnetic triangular motif. Two spins in opposite orientations (black and green) minimize the energy along one bond, however, there is no configuration for the final spin that minimizes energy along both remaining bonds.

typical in these phases [10, 17–19]. QMC algorithm, on the other hand, runs into the infamous fermionic sign problem [20–22]. New, fully-quantum computational tools are required to understand and resolve disputes on how frustration, randomness and distortion influence the ground states in real two-dimensional quantum magnets which are currently explored by neutron scattering and complementary experimental methods such as bulk and thin film susceptibility [23, 24].

Digital and analog quantum simulators have emerged as a new tool for the simulation of quantum many-body phenomena towards efficient modelling of exotic quantum phases of matter beyond classical tractability [25, 26]. They are naturally suited for magnetic Hamiltonians since spin-1/2's can be directly mapped to qubits. Non-trivial phases in magnetic systems have been realized on multiple qubit platforms using a variety of techniques. For example, quantum annealing experiments on programmable superconducting qubits have been performed to access geometrically frustrated phases [27, 28] and spin glass behavior [28]. A topologically ordered phase was also reported on a programmable neutral atom array platform, realizing the elusive quantum spin liquid phase and the coherent quantum transport of information [29]. In a different approach, a universal quantum computer on a superconducting qubit platform has also been used to realize topological order [13].

In this paper, we concentrate on spin-1/2 frustrated magnetic Hamiltonians and analyze the success probability for obtaining the ground state using the quantum approximate optimization algorithm (QAOA) [30] on universal quantum computing hardware. QAOA was originally developed to solve combinatorial optimization problems using a Hamiltonian  $H$  that encodes a classical optimization problem. Typically, the combinatorial  $H$  is expressed in Ising form [31], and can be replaced with a suitable Ising lattice Hamiltonian for materials science applications. While progressing to  $XY$  and Heisenberg models in the fully frustrated limit remains an exciting future goal, here we start in the Ising  $S = \infty$  limit, where standard QAOA is directly applicable.

We solve three different types of Hamiltonians for unit cells pictured in Fig. 2. The first is a square unit cell Hamiltonian, which exhibits only simple ferromagnetic and anti-ferromagnetic phases in the infinite size (thermodynamic) limit. The second is the celebrated Shastry-Sutherland Hamiltonian. Interestingly, this problem already lends itself to materials applications and experimental data analysis, for example, it is conjectured to describe the class of rare-earth tetraborides ( $\text{ErB}_4$ ,  $\text{TmB}_4$  and  $\text{NdB}_4$ ) and allows a direct comparison with several existing results both theoretical [32–36] and experimental [37–42]. The third case is the more complex Ising triangular lattice which represents a maximally frustrated problem in the infinite geometry limit [43, 44]. We compute theoretical probabilities to prepare the ground state for each of these 9-spin Hamiltonians under varying choices of the external field and coupling parameters, and compare these theoretical results against computations on a trapped ion quantum computer. The results demonstrate and quantify the success of QAOA for studying classical materials ground states at small sizes, validating the basic approach for future extensions to larger sizes, more complex Hamiltonians, and generalized algorithms where we may hope to obtain a quantum computational advantage for otherwise intractable materials science applications.

## II. ISING HAMILTONIAN AND MODEL UNIT CELL LATTICES

A single unpaired spin on the outermost orbital of a magnetic ion constitutes a  $s = 1/2$  state which is implemented straightforwardly on a qubit. In a magnetic material, several such spins in a lattice interact via pairwise superexchange interactions  $J_\alpha$ . The nature and strength of these interactions,  $J_\alpha$ , depend on several factors. These include the distance between the magnetic ions (typically scales as the inverse cube of the distance between the ions), the shape of the orbitals, the symmetry of the lattice, and the local crystal fields. Magnetic frustration can arise in the lattice, for example, if spins arranged on a triangular motif in the lattice experience equal Ising antiferromagnetic interactions. On the square lattice, such a magnetic frustration can arise via a combination of straight edge bonds  $J_1$  which are

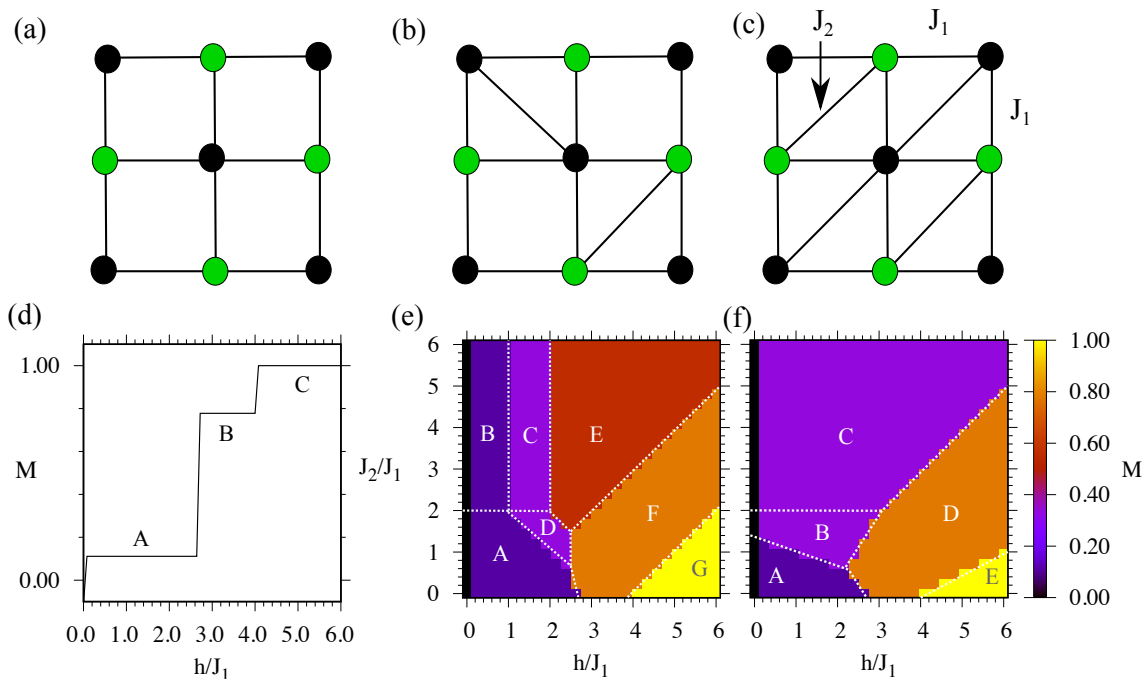


FIG. 2: Unit cells of (a) square, (b) Shastry-Sutherland, and (c) triangular geometries. Colors indicate two spin values  $s_i = \pm 1$  in examples of ground states with  $h/J_1, J_2/J_1, \ll 1$ . (d-f) phase diagrams for each of the unit cells (a-c) respectively, with labels “A”, “B”,... denoting regions with distinct ground states for each lattice. Magnetization  $M = 0$  at  $h = 0$  is due to degeneracy in the ground states, where spin-flip-related pairs of states are present in absence of the field ( $h = 0$ ).

either horizontal or vertical, and the diagonal bonds  $J_2$ . This is given by the Hamiltonian

$$\mathcal{H}(\mathbf{s}) = J_1 \sum_{(i,j) \in \text{NN}} s_i s_j + J_2 \sum_{(i,j) \in \text{NNN}} s_i s_j + h \sum_{i=1}^N s_i, \quad (1)$$

where the first sum is over the nearest neighbors (NN), the second sum is over the diagonal next-nearest neighbors (NNN), and  $\mathbf{s} = (s_1, \dots, s_N)$  lists the spin orientations  $s_i \in \{1, -1\}$  of the  $N$  spins. We study anti-ferromagnetic couplings with positive  $J_1, J_2$ . The term  $h$  represents a longitudinal magnetic field (parallel to the spin axis), which for the real material represents either a mean crystal field or an external magnetic field. The unit cell motif of the Hamiltonian is shown in Fig. 2. The ground states of materials which can potentially comply to this model is being actively researched in condensed matter physics. The Ising Shastry-Sutherland model is a special case of a model, inspired by the geometry of real materials, where some but not all of the diagonal bonds are present (Fig. 2(b)). The triangular lattice is shown in Fig. 2(c).

Obtaining a full understanding of the ground states, even in the Ising limit, requires solving NP-Hard computational problems [45], with exceptions such as when the underlying lattice of Eq. 1 is planar and without a longitudinal field. Multiple methods have been proposed to solve this problem, notably Integer Programming method [46], Simulated Annealing [47] and its variants, Large Neighborhood Search [48] and Quantum or Quantum-inspired physical annealing devices. Among them, the Integer Programming method solves exactly but suffers from exponential scaling of computational time. Simulated Annealing and Large Neighborhood Search are both heuristics methods that promise faster runtime but there is no guarantee of the solution qualities. Quantum annealers, digital annealers and coherent Ising machines are hardware dedicated to solving Ising models [49, 50] but with limitations on problem sizes, connectivity or solution qualities in some cases.

### A. Ground state magnetization phase diagrams

We consider the nine-spin unit cells with geometries in Fig. 2(a-c). These correspond to single components that would be repeated periodically within a very large lattice in a real material. We computed ground states for each

unit cell by evaluating (1) for each possible spin configuration to identify the lowest energy states, for varying choices of  $h$  and  $J_2$ , with  $J_1 = 1$  taken as the unit of energy. We plot the magnetization

$$M = \frac{1}{N} \sum_{i=1}^N s_i, \quad (2)$$

of these ground states in the phase diagrams of Fig. 2(d-f). We further separate each diagram into regions A,B,... with distinct sets of ground states but sometimes equivalent magnetizations. For example, “A” and “B” in Fig. 2(e) have different ground states but identical magnetizations. The individual ground states are shown in the Appendix Figs. 12-14.

The simplest set of ground states is obtained for the square lattice, which does not exhibit frustration as there are no  $J_2$  interactions. The ground states of this lattice (Appendix Fig. 12) are also present in the Shastry-Sutherland and triangular unit cells at small  $J_2$ . At small  $h$  in regions “A”, the ground state is antiferromagnetic with magnetization  $M = 1/9$ , as five spins are aligned with the field while four are anti-aligned. At large  $h$ , the ground state for each lattice is ferromagnetic, in regions C, G, and E in Fig. 2(d-f) respectively. For fields  $8/3 \leq h \leq 4$  and small  $J_2$ , there is a ground state with  $M = 7/9$  in which a single spin in the center of the unit cell is anti-aligned with the field. This state is related to the finite size of the unit cells we study, where the central spin is distinguished as the only spin with four interactions in the square lattice, while all other spins are along the perimeter. In the large size limit there would be nothing to distinguish this central spin from others in the bulk, so we would not expect this ground state based on symmetry, though it is a true ground state for the nine-spin unit cell we consider. As  $J_2$  increases, frustration leads to a variety of different ground states for the Shastry-Sutherland and triangular lattices, with varying magnetizations in Fig. 2(e-f), with ground states in Figs. 13-14.

### B. Small size effects

The small sizes of our lattice unit cells, as well as the unusual  $M = 7/9$  ground state noted in the previous section, raise questions of how the ground states for our unit cells match with ground states that would be obtained in the large size limit, and the minimum number of spins that are needed to achieve quantitative behavior consistent with large sizes. To address these questions, we computed the magnetization of triangular and Shastry-Sutherland lattices of  $N = n \times n$  spins to analyze the size-dependent behavior. Due to the exponential complexity of the problem, we used *neal* [51], a software implementation of simulated annealing to approximate the ground state configurations with  $h, J_2 \in [0, 6]$  and  $J_1 = 1$ . Each combination of  $h$  and  $J_2$  was run 50 times and the solution with minimum Ising energy was picked. Examples with  $3 \leq n \leq 30$  are shown in Fig. 3. We assessed convergence of the global phase diagrams to the large size limit by computing the root mean square error (RMSE) between the target lattice’s and  $30 \times 30$  lattice’s magnetization across points in the phase diagram and fitted them to an empirical exponential function of the form

$$\text{RMSE}(M_{n \times n}, M_{30 \times 30}) = \sqrt{\frac{\sum_g (M_{n \times n, g} - M_{30 \times 30, g})^2}{\mathcal{N}}} \approx a e^{-bn}. \quad (3)$$

where  $\mathcal{N} = 900$  is the number of points  $g$  we evaluated in each phase diagram (30 evaluations for  $h \in [0, 6]$  and 30 evaluations for  $J_2 \in [0, 6]$  with a step size of 0.2 in each variable). The computed RMSEs and fitted curves are shown in Fig. 4. Empirically, the RMSE converges exponentially towards zero, demonstrating that a  $15 \times 15$  spin grid is already obtaining results close to the much larger  $30 \times 30$  grid. Based on this trend we expect that small size effects in  $M$  will vanish exponentially with the size of the lattice, indicating that lattices of only a few hundred spins may be necessary to achieve a realistic “bulk”, and therefore meaningful results for comparison with experiments which probe bulk properties, such as diffraction and heat-capacity. This suggests that quantum processors with hundreds of qubits, achievable within the noisy intermediate-scale quantum era [52], will be capable of meaningful applications for materials science applications.

## III. QUANTUM APPROXIMATE OPTIMIZATION ALGORITHM

Quantum computers offer a route to overcoming issues associated with identifying ground states through conventional methods. One approach to address these problems uses the quantum approximate optimization algorithm, which was originally designed to find approximate solutions to difficult combinatorial optimization problems [30] that are often expressed in terms of Ising Hamiltonians [31]. Empirical performance of QAOA has been characterized for a variety of combinatorial problems [53–57] and this has also led to generalizations [58–63] that have been applied to

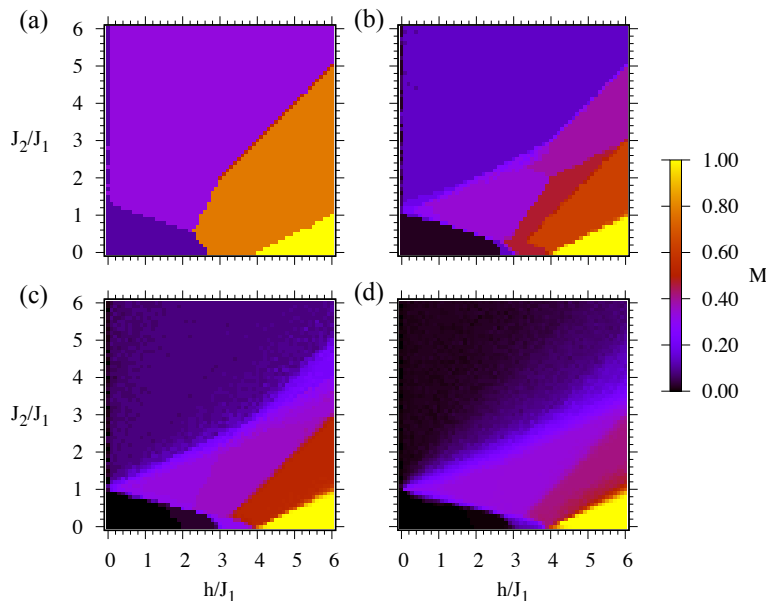


FIG. 3: Ground state magnetization of  $n \times n$  triangular spin arrays with a number of spins per dimension (a)  $n = 3$ , (b)  $n = 7$ , (c)  $n = 12$ , and (d)  $n = 30$ , computed as described in Sec. II B.

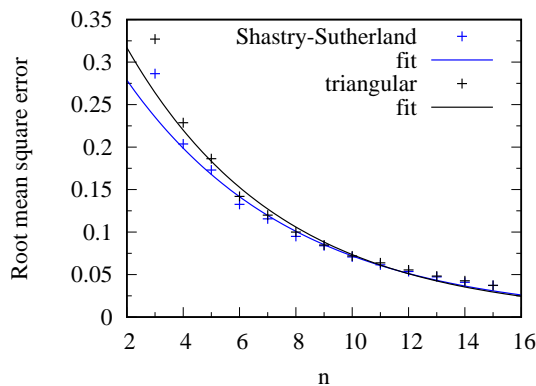


FIG. 4: Root mean square errors (3) of total magnetization between  $n \times n$  lattices relative to a  $30 \times 30$  lattice. Solid lines show non-linear least squares fits at  $n \geq 4$ , with  $a = 0.45 \pm 0.02$ ,  $b = 0.182 \pm 0.007$  for the triangular lattice and  $a = 0.39 \pm 0.02$ ,  $b = 0.169 \pm 0.006$  for the Shastry-Sutherland lattice in (3), with  $\pm$  the asymptotic standard error of the fit parameters. The higher RMSE error for the triangular lattice at small  $n$  may be due to a higher degree of frustration as compared to the Shastry-Sutherland model. The later has half of the  $J_2$  diagonal bonds equal to zero relieving some of the frustration.

preparing chemical ground states [64] as well as ground state preparation for one-dimensional quantum spin models in theory [65, 66] and experiment [67].

To formulate our Ising problems in a structure that is suitable for QAOA, we first express the Ising Hamiltonian (1) in terms of a quantum Hamiltonian operator

$$H = J_1 \sum_{(i,j) \in \text{NN}} Z_i Z_j + J_2 \sum_{(i,j) \in \text{NNN}} Z_i Z_j + h \sum_{i=1}^N Z_i. \quad (4)$$

Here the spins  $s_i \in \{+1, -1\}$  in (1) are encoded into the eigenvalues of the Pauli  $Z$  operators, with  $Z_i |z_i\rangle = s_i |z_i\rangle$ , where  $z_i \in \{0, 1\}$  and  $s_i = 1 - 2z_i$ . The set of all spin values is then encoded into a computational basis state  $|\mathbf{z}\rangle = \bigotimes_{i=1}^N |z_i\rangle$ . Each  $|\mathbf{z}\rangle$  is an energy eigenstate of  $H$  with the energy eigenvalue of the corresponding classical spin

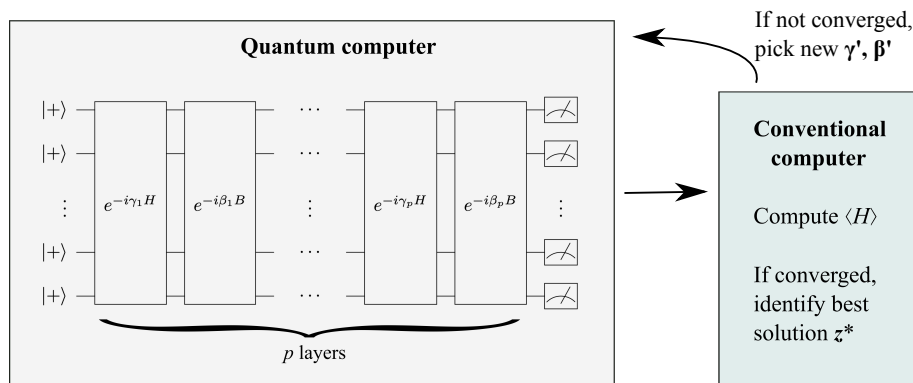


FIG. 5: Quantum-classical optimization loop for QAOA. For a given set of parameters  $\gamma, \beta$ , a quantum computer generates and measures states  $|\psi_p(\gamma, \beta)\rangle$ . The measurements are sent to a conventional computer to compute  $\langle H \rangle$  and check its convergence. If  $\langle H \rangle$  is not converged, then an optimization routine selects new  $\gamma'$  and  $\beta'$  for the quantum computer. If  $\langle H \rangle$  is converged, then the algorithm terminates and the final solution is the measured result  $z^*$  that minimizes the energy.

problem,

$$H|z\rangle = \mathcal{H}(z)|z\rangle, \quad (5)$$

where  $\mathcal{H}(z)$  comes from (1) taking  $s_i = 1 - 2z_i$  for each component  $|z_i\rangle$  in the total basis state  $|z\rangle$ . This gives an encoding of the Ising spin problem (1) that is useful for QAOA, where we will sample eigenstates  $|z\rangle$  to try to identify the ground state of the Ising problem.

To find solutions, QAOA uses a quantum state prepared with  $p$  layers of unitary evolution, where each layer alternates between Hamiltonian evolution under the Ising Hamiltonian  $H$  and under a “mixing” Hamiltonian  $B = \sum_i X_i$

$$|\psi_p(\gamma, \beta)\rangle = \left( \prod_{l=1}^p e^{-i\beta_l B} e^{-i\gamma_l H} \right) |\psi_0\rangle \quad (6)$$

where the initial state  $|\psi_0\rangle = 2^{-N/2} \sum_{\mathbf{z}} |\mathbf{z}\rangle$  is the ground state of  $-B$  represented in the computational basis. The parameters  $\gamma = (\gamma_1, \dots, \gamma_p)$  and  $\beta = (\beta_1, \dots, \beta_p)$  are typically chosen to minimize the expectation value of the energy  $\langle H \rangle$ , though other objectives have also been studied [64, 68, 69]. The minimization is typically accomplished using a quantum-classical hybrid feedback loop, shown schematically in Fig. 5. For a given set of parameters  $\gamma$  and  $\beta$ , a set of states  $|\psi_p(\gamma, \beta)\rangle$  is prepared and measured by a quantum computer. The measurement results are sent to a conventional (classical) computer to compute the classical objective function. If the objective function is not converged relative to previous evaluations, then the conventional computer uses an optimization routine to select new parameters  $\gamma', \beta'$ . The process is repeated until convergence to a minimal objective with optimized parameters  $\gamma^*, \beta^*$ . The final result is taken as the measurement result  $|z^*\rangle$  that gives the lowest energy  $\mathcal{H}(z^*)$ . In the best case,  $z^* = z_{\text{ground}}$  is a ground state, while more generally  $z^*$  may be a low-energy state that is an approximate solution to the problem.

An analytic proof has demonstrated that QAOA can prepare an exact ground state  $|z_{\text{ground}}\rangle$  of Ising Hamiltonians as  $p \rightarrow \infty$  [30, 31]. Apart from the formal proof of convergence at large  $p$ , there has been significant interest in applying QAOA at small  $p$ , where approximations exceeding conventional lower bounds have been observed in simulations [53, 70] and predicted for large problems in certain contexts [71]. Realizing such advantages on devices with hundreds of qubits or more is an important topic of ongoing research as quantum computing technologies continue to develop.

For the materials problems we consider, we are interested in preparing the ground state of the Ising Hamiltonian. We compute exact ground states for our unit cells in Fig. 2 by evaluating all eigenvalues of the Hamiltonian using Eqs. (1) and (4) to identify the lowest energy state. To assess QAOA performance, we compute the average ground state probability

$$\overline{P}_{\text{ground}} = \frac{1}{N_{\text{ground}}} \sum_{z_{\text{ground}}} P(z_{\text{ground}}), \quad (7)$$

where  $N_{\text{ground}}$  is the number of ground states  $z_{\text{ground}} \in \arg \min_{\mathbf{z}} \mathcal{H}(\mathbf{z})$ , with the sum accounting for the potential to have degenerate ground states. Analytically, the probabilities are given by the Born rule  $P(z) = |\langle z | \psi_p(\gamma, \beta) \rangle|^2$ , while

for experiments on a quantum computer they are given by the frequencies of measurement results,  $P(\mathbf{z}) = N(\mathbf{z})/N_{\text{tot}}$ , where  $N(\mathbf{z})$  is the number of times  $|\mathbf{z}\rangle$  was measured and  $N_{\text{tot}}$  is the total number of measurements. If QAOA identifies a ground state then  $|\mathbf{z}^*\rangle = |z_{\text{ground}}\rangle$  and  $\overline{P}_{\text{ground}} > 0$ , while if QAOA only finds sub-optimal solutions then  $\overline{P}_{\text{ground}} = 0$ .

Ground state preparation is a goal specific to the materials problem context we are interested in here. This is, importantly, a departure from the standard goal of QAOA in the context of approximate combinatorial optimization, where the goal is to find approximate solutions that are not necessarily the ground states. While QAOA is not expected to efficiently find exact ground states for generic NP-hard optimization problems, it can still prove useful for finding ground states of specific structured problems such as materials problems on a lattice similar to those we explore here [65–67].

### A. Numerical simulations of ideal QAOA

We use numerical calculations to assess the theoretical performance of QAOA for ground state preparation. These demonstrate the ideal performance of QAOA in exact pure state calculations that use matrix multiplication to evaluate (6). This gives an ideal baseline for later comparison against results from a noisy quantum computer, where errors lead to mixed states with degraded performance. We use  $p = 1$  QAOA layers throughout this section and our results.

To identify QAOA states for our Ising problems we must determine optimized QAOA parameters  $\gamma_1^*$  and  $\beta_1^*$ . We choose regions to evaluate parameters in determining  $\gamma_1^*$  and  $\beta_1^*$  as follows. QAOA is periodic when  $\beta_1 \rightarrow \beta_1 \pm \pi$  [54], hence we consider  $-\pi/2 \leq \beta_1 \leq \pi/2$ , which gives all unique  $\beta_1$  up to symmetries. The periodicity of the  $\gamma_1$  parameter is more complicated, as it depends on the Hamiltonian in  $\exp(-i\gamma_1 H)$  in (6). Here we focus on  $\gamma_1$  intervals near the origin and dependent on the magnitude of the Hamiltonian terms, which has been highly successful in previous work [72]. The basic idea is that the QAOA unitary  $\exp(-i\gamma_1 H)$  changes at varying speeds with respect to  $\gamma_1$ , depending on the Hamiltonian coefficients  $J_1$ ,  $h$ , and  $J_2$ . When the Hamiltonian coefficients increase, then  $\gamma_1$  should decrease to obtain a similar unitary. The rate at which the unitary changes with respect to  $\gamma_1$  is related to the average magnitude of the Hamiltonian coefficients

$$\iota = \frac{Nh + J_1 E_{\text{NN}} + J_2 E_{\text{NNN}}}{N + E_{\text{NN}} + E_{\text{NNN}}}, \quad (8)$$

where  $E_{\text{NN}}$  is the number of nearest-neighbor interactions and  $E_{\text{NNN}}$  is the number of next-nearest-neighbor interactions. Previous work on generic Ising Hamiltonians with  $h = 0$  has shown that high quality solutions are obtained at small  $\gamma_1$  with an empirical scaling of optimized parameters similar to  $\gamma_1^* \sim 1/\iota$ . The scaling  $1/\iota$  compensates for the varying rates of evolution that are present for varying choices of the Hamiltonian, and also limits the interval of  $\gamma_1$  values that are explored, simplifying the optimization [72]. Based on these ideas we choose  $\gamma_1$  in the interval  $-\pi/2\iota \leq \gamma_1 \leq \pi/2\iota$  for our calculations.

We show an example of how the energy expectation value and average ground state probability depend on the choice of parameters in Fig. 6 for an example with the Shastry-Sutherland unit cell with Hamiltonian coefficients  $J_1 = 1$ ,  $J_2 = 3.7$ , and  $h = 1.4$  (similar patterns are observed in sample calculations using other choices of Hamiltonian coefficients and also for the triangular unit cell). There are two regions in Fig. 6(a) with optimized  $\langle H \rangle$  in yellow. The ground state probabilities in Fig. 6(b) are also relatively large near the  $\gamma_1^*$  and  $\beta_1^*$  that optimize  $\langle H \rangle$ .

We have found in searches over much larger  $\gamma_1$  intervals that the local optima for  $\overline{P}_{\text{ground}}$  and  $\langle H \rangle$  do not always approximately align as in Fig. 6, which can lead to poor  $\overline{P}_{\text{ground}}$  at optimized  $\langle H \rangle$  in these larger intervals. However, this does not appear to be a prevalent issue for the smaller  $\iota$ -dependent  $\gamma_1$  intervals in cases we have looked at.

To identify optimized parameters, we perform a grid search over  $\gamma_1$  and  $\beta_1$  for each Hamiltonian considered. We evaluate the QAOA states in (6) on 201 evenly spaced intervals with  $-\pi/2 \leq \beta_1 \leq \pi/2$  and over 300 evenly spaced intervals with  $-\pi/2\iota \leq \gamma_1 \leq \pi/2\iota$  for a total of  $201 \times 300 = 60,300$  grid evaluations for each Hamiltonian. This approach gives optimal parameters in our intervals up to coarse graining in the grid search. We select parameters the  $\gamma_1^*$  and  $\beta_1^*$  that optimize  $\langle H \rangle$ .

The optimized parameters  $\gamma_1^*$  and  $\beta_1^*$  do not necessarily give the optimal ground state probabilities that are possible from QAOA. The reason is that the average energy optimization accounts for energies and probabilities of all states, which together may yield low energies at parameter choices that are not optimal for the ground states alone [53]. To assess performance, we further compare our parameter choices against parameters  $\gamma_1^{*'}$  and  $\beta_1^{*'}$  that directly optimize  $\overline{P}_{\text{ground}}$ . The direct optimization of  $\overline{P}_{\text{ground}}$  is used here for benchmarking purposes and is not a realistic approach for large problems where the ground states are unknown. For our small problems, the comparison gives an idea of how the ground state probabilities from a standard optimization of  $\langle H \rangle$  compare against the best ground state probabilities that could be obtained by QAOA in our setup.

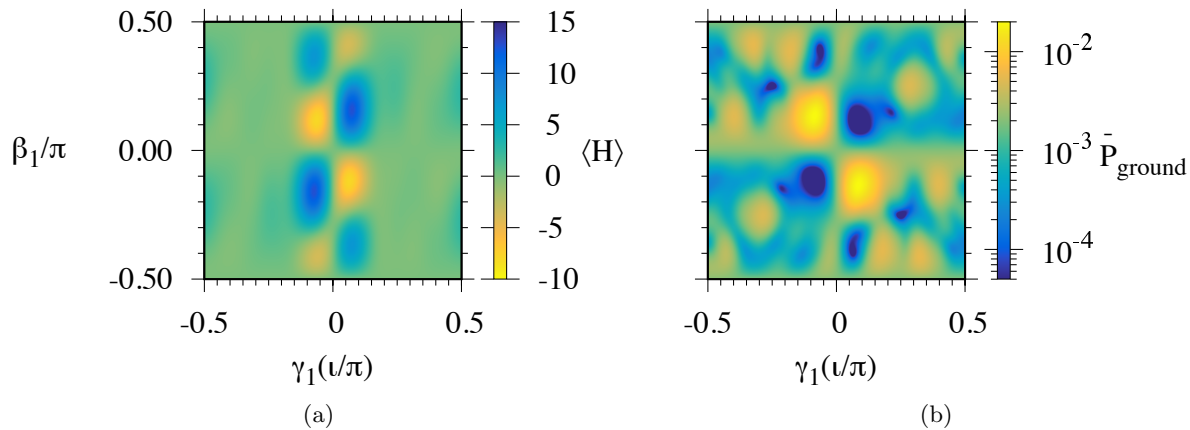


FIG. 6: Numerical simulations of the (a) average energy  $\langle H \rangle$  and (b) average ground state probability  $\bar{P}_{\text{ground}}$  with varying choices of QAOA parameters  $\gamma_1$  and  $\beta_1$ , for the Shastry-Sutherland unit cell with  $J_1 = 1$ ,  $J_2 = 3.7$ , and  $h = 1.4$  (Sec. III A). Each plot has the same range of  $\beta_1$  and  $\gamma_1$ ; the color scales are reversed in (a) and (b) so that small  $\langle H \rangle$  and large  $\bar{P}_{\text{ground}}$  are each represented by bright colors.

## B. Quantum computations of QAOA

We next investigate the performance of QAOA using the Quantinuum H1-2 quantum computer. H1-2 contains trapped-ion qubits and uses lasers to implement gates on these qubits. Typical error rates are reported as  $3.5 \times 10^{-3}$  for two-qubit gates and  $1 \times 10^{-4}$  for single-qubit rotation gates [73]. In addition to the device H1-2, we also use the H1-1E device “emulator” to simulate noisy device behavior. This gives results that approximately correspond to expected device behavior while avoiding the financial expense and wait times that are associated with running the device. The emulator models a variety of device-specific noise processes for the H1-class computers, including depolarizing noise, leakage errors, crosstalk, dephasing in transport, and qubit idling errors [74].

We test QAOA on the H1-2 using the QCOR software stack [75]. The QCOR stack translates the series of unitary operators expressing QAOA into quantum circuits for H1-2; see Appendix A for details. The QCOR program used for submitting jobs to the device as well as our calculations are available online, cf. “Data Accessibility”.

Furthermore, modern quantum computers are known to be affected by state preparation and measurement (SPAM) errors as well as gate infidelities from a variety of physical sources. We assessed SPAM errors expected in our quantum computations using the device emulator, with details in Appendix B. The probability to observe no error in circuits we tested was approximately 96%, with errors distributed approximately uniformly across qubits. We account for these errors using an independent bit-flip model and associated SPAM matrix  $\hat{P}$ , which transforms an ideal set of measurement results to the expected noisy set of results. The inverse matrix  $\hat{P}^{-1}$  can then be applied to our noisy measurements from the quantum computer to approximately correct for SPAM errors. A technical issue arises in that the mitigated measurement probabilities can sometimes be negative, due to the approximate nature of the mitigation scheme. This leads to a second mitigation scheme that additionally sets all negative probabilities to zero and renormalizes so the total probability is one. We use each of these approaches to attempt to correct the small SPAM errors we expect from the quantum computer, as described in detail in Appendix B.

## IV. RESULTS

In this section we consider the results from QAOA applied to the materials lattices of Fig. 2. We take  $J_1 = 1$  as the unit of energy and analyze the success of QAOA in preparing ground states at variable  $h$  and  $J_2$ , first in numerical simulations (Sec. III A) and then in quantum computations on a trapped-ion quantum computer (Sec. III B).

### A. Ground state measurement probabilities

We first consider theoretical probabilities to measure the ground state with QAOA and how these vary for different parameter choices in the Hamiltonian. We begin with the simple square lattice in Fig. 2(a,d), which does not exhibit frustration as there are no triangles in the interaction graph. The probability to measure the ground state for varying



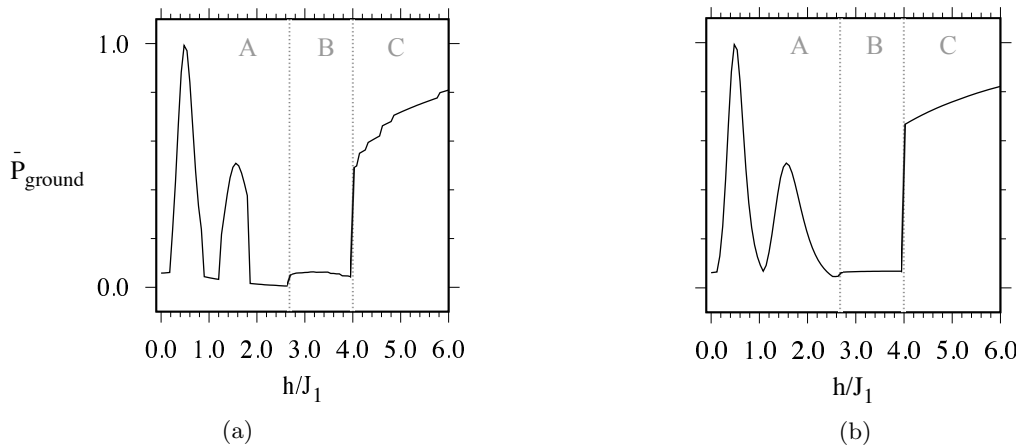


FIG. 7: The square unit cell ground state probabilities when (a) optimizing  $\langle H \rangle$  and (b) optimizing  $\overline{P}_{\text{ground}}$  as described in Sec. III A. The  $\overline{P}_{\text{ground}}$  ranges are identical in each figure.

$h$  is shown in Fig. 7. Fig. 7(a) shows the probabilities obtained from optimizing the standard objective  $\langle H \rangle$  while Fig. 7(b) shows the best-case results based on optimizing  $\overline{P}_{\text{ground}}$ , as described in Sec. III A. The probabilities in each case are similar, demonstrating that optimizing  $\langle H \rangle$  is nearly as successful in increasing the ground state probability as a direct optimization.

The average ground state probability shows distinct behaviors for each of the three ground states at varying  $h$ , visually separated by dotted lines. In the antiferromagnetic ground state at small  $h$ , the probability  $\overline{P}_{\text{ground}}$  approximately oscillates between  $h = 0$  and  $h = 2$ , with small probabilities observed near integer values of  $h$  and larger probabilities at  $h = 1/2$  and  $h = 3/2$ . The  $M = 7/9$  ground state with  $8/3 \leq h \leq 4$  has a near-constant probability of  $\approx 0.06$ . At  $h = 4$  the ground state becomes ferromagnetic and  $\overline{P}_{\text{ground}}$  increases significantly, with monotonic increases at larger  $h$ .

We rationalize the varying success probabilities in the figure as attributable to structures of the ground states at varying  $h$  and the interplay with the structure of the QAOA state in (6). We present a straightforward argument in Appendix C that QAOA can exactly prepare the ferromagnetic ground state when  $h \gg J_1$ , based on the fact that  $\exp(-i\gamma H) \approx \exp(-i\gamma h \sum_{i=1}^N Z_i)$  in this limit. This is consistent with the behavior in the figure, where  $\overline{P}_{\text{ground}}$  increases monotonically with  $h$  for the ferromagnetic ground state at  $h \geq 4$ . In contrast, preparing the antiferromagnetic and  $M = 7/9$  ground states requires QAOA dynamics that rely on an interplay of the  $h$  and  $J_1$  components in the total evolution  $\exp(-i\gamma H)$ . The success probability depends on how well these dynamics can create the corresponding ground states and may be sensitive to the values of  $h$  and  $J_1$ , as is evident in the oscillations in  $\overline{P}_{\text{ground}}$  at small  $h$ .

Ground state probabilities  $\overline{P}_{\text{ground}}$  for the Shastry-Sutherland and triangular lattices are pictured in Figs. 8 and 9, respectively. Ground state probabilities from optimizing  $\langle H \rangle$  are presented in panels (a) while panels (b) show the best case probabilities from a direct optimization of  $\overline{P}_{\text{ground}}$  as described in Sec. III A. These probabilities show patterned behavior, with distinct probabilities  $\overline{P}_{\text{ground}}$  observed throughout most of each individual region A, B, ..., with significant differences in  $\overline{P}_{\text{ground}}$  between different regions. At small  $J_2$ , there are oscillations in the probability for preparing the anti-ferromagnetic ground states at small  $h$ , and large success probabilities for the ferromagnetic ground at large  $h$ , as foreshadowed by results from the square lattice. On the other hand, as the  $J_2$  coupling increases, the triangular and Shastry-Sutherland lattices experience increased frustration, with competing interactions within the triangular motifs in Fig. 2. The average ground state probability decreases significantly as  $J_2$  increases and frustration becomes dominant. This is especially evident when  $J_2 \gtrsim h$ , for example in the top left of each of Figs. 8(b) and 9(b). The  $\overline{P}_{\text{ground}}$  are mostly uniform across  $h$  and  $J_2$  within each region, qualitatively similar to the nearly-uniform probability for the  $M = 7/9$  state at varying  $h$  for the square lattice in Fig. 7. Ground state probabilities are typically  $\gtrsim 0.01$ , indicating that only  $\lesssim 100$  measurements are expected to identify a ground state. We now turn to computations on a trapped-ion quantum computer, to benchmark and assess performance of QAOA on a real quantum computing device.

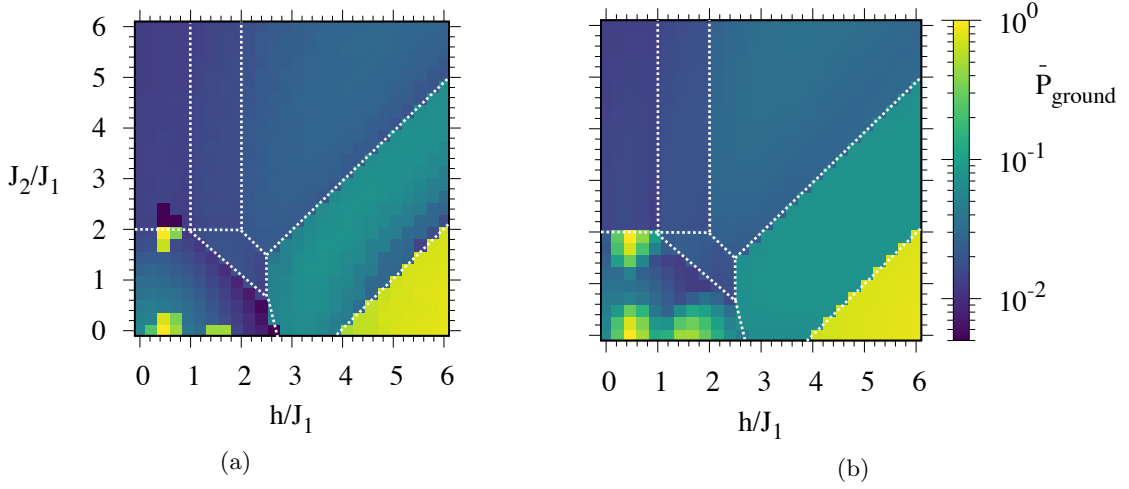


FIG. 8: Shastry-Sutherland unit cell ground state probabilities when (a) optimizing  $\langle H \rangle$  and (b) optimizing  $\bar{P}_{\text{ground}}$  as described in Sec. III A. The ranges for  $J_2/J_1$  and  $\bar{P}_{\text{ground}}$  are identical in each figure.

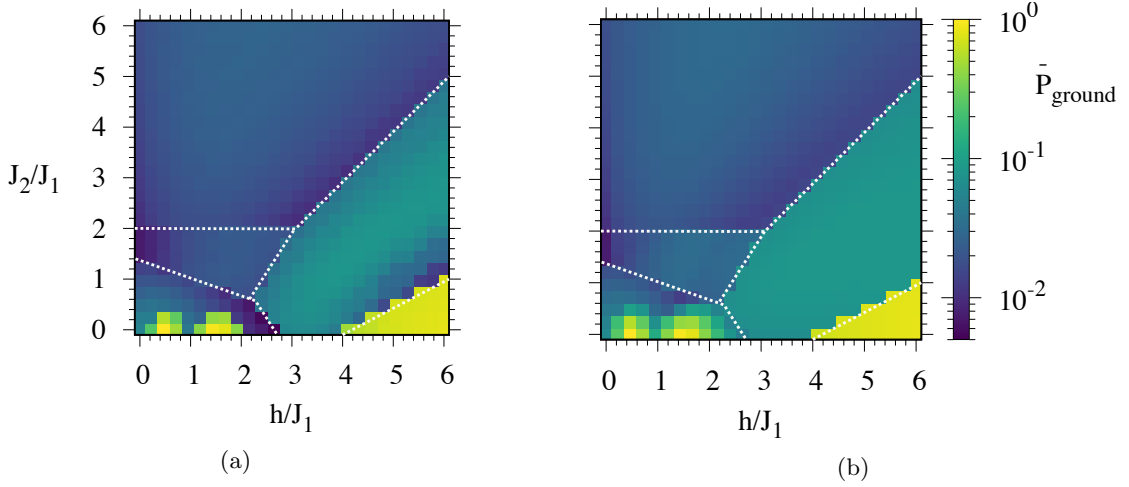


FIG. 9: Triangular unit cell ground state probabilities when (a) optimizing  $\langle H \rangle$  and (b) optimizing  $\bar{P}_{\text{ground}}$  as described in Sec. III A. The ranges for  $J_2/J_1$  and  $\bar{P}_{\text{ground}}$  are identical in each figure.

## B. QAOA quantum computations

Here we assess QAOA performance in preparing ground states on a trapped-ion quantum computer. Ultimately, our aim is to validate the idea that a current quantum computing technology is capable of preparing each ground state of a frustrated Ising Hamiltonian using QAOA. An important first step is to assess whether optimized parameters from our theoretical calculations are also optimized for the device, or whether further optimization is needed to determine device-specific optimized parameters.

### 1. Quantum computational performance with varying parameters

QAOA depends on the choice of parameters, as discussed in connection with Fig. 6. To test whether our theoretical parameters also yield good performance in the device, we consider QAOA circuits evaluating a point in region E of the Shastry-Sutherland phase diagram Fig. 2(e), with Hamiltonian coefficients and QAOA parameters shown in Table I. The parameters correspond to a local minimum in  $\langle H \rangle$ , similar to the minima observed in Fig. 6. We use the H1-1E device emulator to evaluate circuits at the optimized  $\gamma_1$  and  $\beta_1$  and circuits where either  $\gamma_1$  or  $\beta_1$  has been displaced from its optimal value, as shown in Fig. 10. Black crosses in the figure indicate how  $\langle H \rangle$  increases in pure state

region	degeneracy	$M$	$J_2/J_1$	$h/J_1$	$\beta_1/\pi$	$\gamma_1/\pi$	$N_{\text{shots}}$
A	1	1/9	0.240	1.440	0.750	-0.507	400
B	4	1/9	3.840	0.480	0.112	-0.048	1000
C	4	3/9	3.840	1.680	0.121	-0.043	1000
D	2	3/9	1.680	1.920	0.131	-0.056	400
E	4	5/9	2.000	2.480	0.143	-0.050	1000
F	1	7/9	1.680	3.600	0.182	-0.046	400
G	1	1.0	0.240	5.520	0.244	-0.041	400

TABLE I: The parameters used for quantum computations with the Shastry-Sutherland lattice. Here  $J_2/J_1$  and  $h/J_1$  are the Hamiltonian coefficients used in the calculations,  $\gamma$  and  $\beta$  are the QAOA parameters, and  $N_{\text{shots}}$  is the number of measurement shots taken on the quantum computer.

simulations as either of these parameters are varied individually. Error bars denote the analytic standard error of the mean (S.E.M.) for  $N_{\text{shots}} = 1000$  measurement shots, with  $\text{S.E.M.} = \sqrt{(\langle H^2 \rangle - \langle H \rangle^2)/N_{\text{shots}}}$  calculated analytically from the pure states. If the quantum computations did not have any noise, then from the central limit theorem we would expect about two-thirds of the  $\langle H \rangle$  from the quantum computer to be within these error bars.

The theoretical  $\langle H \rangle$  can be compared against the device emulator, with data point labels in the figure beginning with “H1-1E”. There are three sets of data points for the emulator; the first is direct output labeled “H1-1E”, the second includes SPAM error mitigation (Sec. IIIB and Appendix B) in “H1-1E, E.M.”, the third includes a variation of the SPAM mitigation that additionally forces the mitigated probabilities to be  $P \geq 0$  in “H1-1E, E.M.,  $P \geq 0$ ”. These emulated  $\langle H \rangle$  are larger than the theoretical values and we attribute this to noise in the device emulator, which introduces errors that cause the energy to deviate from its ideal minimum value. Despite these errors, the shape of the landscape is similar to our theoretical calculations, with best performance observed near the theoretical parameters that minimize  $\langle H \rangle$ , and energies that tend to increase away from these parameters.

We further validate that the H1-2 trapped-ion device itself is consistent with the emulator in the data points that begin with “H1-2”. These actually yield better energies than the emulator, and are within one standard error of the mean from our theoretical results. The results from the device and emulator indicate that the energy landscape as a function of the QAOA parameters  $\gamma_1$  and  $\beta_1$  is consistent between our theoretical calculations, the quantum device, and emulator. We therefore proceed with our theoretically optimized parameters to evaluate success in ground state preparation using the quantum computer.

## 2. Quantum calculations of ground states

We now perform calculations on the Honeywell H1-2 quantum computer to analyze success probability in ground state preparation. We consider points in each region of the Shastry-Sutherland lattice, using parameters listed in Table I that correspond to local minima in  $\langle H \rangle$ , similar to the minima used to evaluate theoretical performance in Sec. IV A). We post-process the measurement results using the SPAM mitigation model with probabilities  $P(\mathbf{z}) \geq 0$  (Appendix B), to give a minor correction to the observed results that is designed to counteract this known source of error.

Figure 11 shows the ground state probabilities from quantum computations in comparison with ideal expectations from pure states. The ground states are separated by regions A,B,... with markers a,b,... corresponding to the individual ground states pictured in Fig. 13. The quantum computations succeed in observing each individual ground state in each region of the Shastry-Sutherland lattice, as seen by the positive probabilities in each state “a”, “b”, ...

For a closer comparison of probabilities, we plot error bars denoting the theoretical standard error of the mean  $\text{S.E.M.} = \sqrt{P(\mathbf{z})(1 - P(\mathbf{z}))/N_{\text{shots}}}$ . The S.E.M. defines a range in which we expect about two-thirds of estimated  $P_{\text{est}}(\mathbf{z}) = N(\mathbf{z})/N_{\text{shots}}$  are expected to be found, where  $N(\mathbf{z})$  is the number of measurement results of a given ground state and  $N_{\text{shots}}$  is the total number of measurements in Table I. The probabilities from the quantum computation are largely consistent with the pure state results, with the majority of results within one S.E.M. from the ideal  $P(\mathbf{z})$ , as expected in finite sampling to estimate the ground state probability. There are only two large deviations for states “k” and “i”, which may be related to noise in the device. The quantum computations succeed in preparing and ground states with probabilities comparable to pure-state expectations.

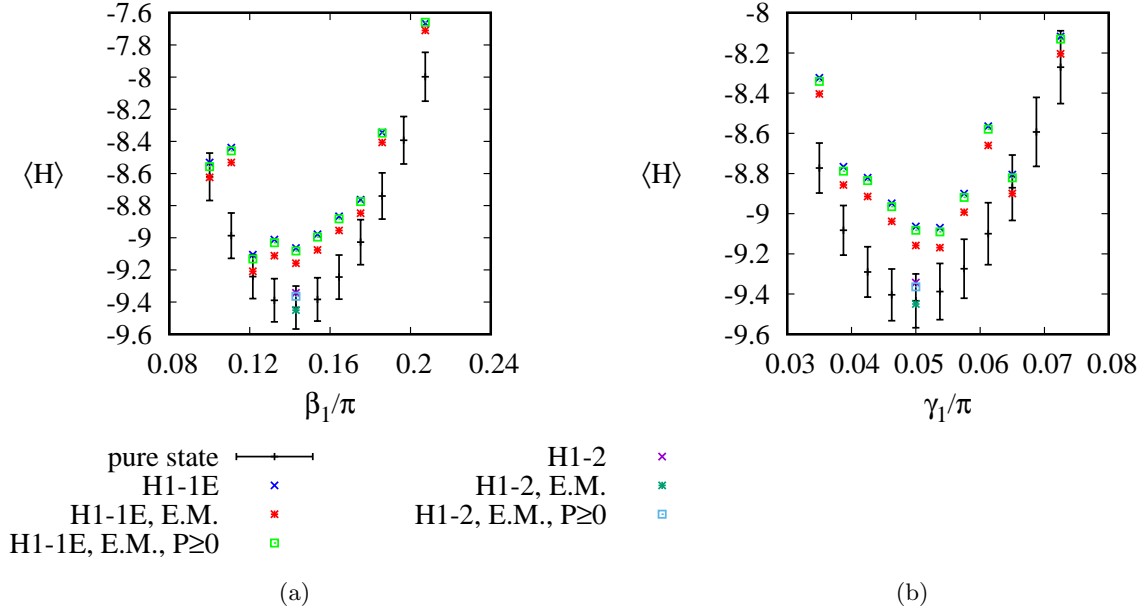


FIG. 10: Angle sensitivity analysis for  $h = 2.48$  and  $J_2 = 2.0$ , with separate variations in (a)  $\beta_1$  and (b)  $\gamma_1$  about the ideal values from Table I. Black crosses show results from pure state calculations, with error bars denoting the standard error of the mean at 1000 shots (see text). Data points showing results from the Honeywell emulator are denoted with “E” in H1-1E and results from the trapped-ion quantum computer are labeled H1-2. Data points labeled “H1-1E” and “H1-2” are raw data, labels “E.M.” (error-mitigation) are with basic mitigation, and “E.M.  $P \geq 0$ ” are readout error mitigation that forces each probability  $P(\mathbf{z})$  to be  $\geq 0$ , as described in Sec. III B and Appendix B.

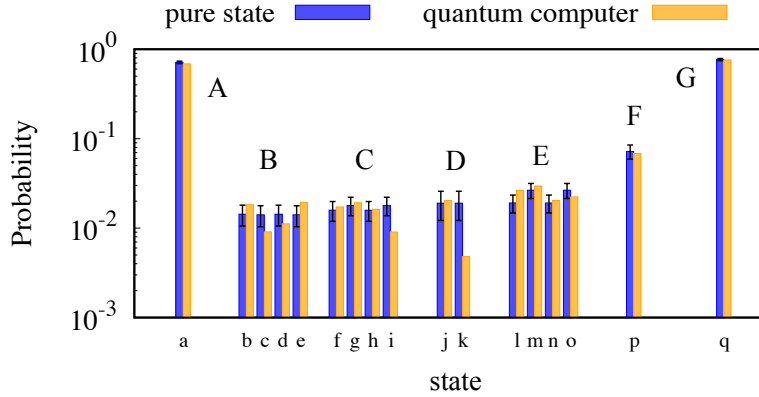


FIG. 11: Probabilities to observe each ground state from pure state simulations compared with observed frequencies estimated by quantum computations with the H1-2 device for each different phase (A-G) of the Shastry-Sutherland unit cell. Alphabetical labels “a”, “b”, etc., identify the different ground states in Fig. 13.

## V. CONCLUSION

We analyzed QAOA as an approach for preparing materials ground states on three types of Ising Hamiltonians with longitudinal magnetic fields, focusing on nine-spin unit cells as a starting size that is amenable to simulations and calculations on a trapped-ion quantum computer.

We applied QAOA to the nine-spin Ising unit cell problems to assess its success in ground state preparation. We found that the theoretical success probability depends significantly on the structure of the ground state, while it is mostly insensitive to the precise Hamiltonian parameters, which can vary within regions consistent with a fixed ground state. Each Hamiltonian yields a ferromagnetic ground state in the presence of large magnetic fields, and QAOA achieved large success probabilities for these relatively simple states. The probabilities for other types of

ground states were more variable, and tended to decrease as next-nearest-neighbor couplings became stronger with associated frustration in the lattice. For all of these nine-spin states, we typically find success probabilities indicating that  $\lesssim 100$  measurements are expected to be necessary from an ideal quantum computer for these problem instances.

To assess QAOA performance under realistic conditions we implemented the algorithm on a trapped-ion quantum computer. These quantum computations succeeded in observing each of the 17 ground states of the Shastry-Sutherland unit cell. The quantum computations yielded ground state probabilities that were consistent with theoretical expectations based on pure states, indicating that noise was not a significant issue at the sizes and depths tested. This suggests that calculations with current technology can likely be extended to greater QAOA depth parameters  $p$ , and to larger sizes as greater numbers of qubits become available. At greater depths and sizes we expect higher performance and more realistic results in comparison with the large size limit, respectively.

While the ground states and associated phase diagrams for our nine-spin unit cells were found to have significant finite size effects relative to the large-size limit, the errors from finite size effects on the classically-calculated magnetization phase diagrams on  $n \times n$  lattices up to  $n = 30$  was found to be suppressed exponentially with  $n$ , with small errors at  $n = 15$  indicating that only hundreds of spins may be necessary to reproduce large scale behavior. This provides a baseline of hundreds of qubits for quantum computational experiments that seek to explain materials science problems, which may be accessible to near-term quantum computers in coming years.

Thus we envision QAOA can be successfully applied to larger lattice problems as quantum computing technologies develop and larger number of qubits become available. These could be used for optimization of Ising lattice problems as we have here, with increasing sizes that describe real bulk properties of materials in the  $N \rightarrow \infty$  limit. We expect the number of QAOA layers  $p$  will need to increase with  $N$  to maintain a significant success probability for these applications, and analyzing the dependence on  $p$  and  $N$  is an important topic for future research. But a more promising future direction leveraging the full benefit of this approach is to extend and modify QAOA to prepare ground states of quantum Hamiltonians such as the  $XY$  and Heisenberg models, which can lead to a variety of quantum phenomena not captured in the Ising model, such as quantum spin glasses [76], spin nematicity [77], Berzinski-Kosterlitz-Thouless states [78, 79] and long-range entangled states such as Dirac string excitations [80], the likes of which exist in 2D frustrated quantum spin liquids and spin ice. Many of these topics are fiercely researched and are of considerable interest and importance for future quantum technologies and devices. Conventional numerical methods for understanding these states are hindered by the exponential size of the Hilbert space, making it difficult to generate a theoretical understanding of experimental observations. QAOA or related generalizations [58, 64–67] offer a promising route to overcome conventional computing bottlenecks. Some successes along these lines have been observed in certain contexts, however, advances in methodology and quantum computing technologies are needed to extend these methods to complicated and larger-scale problems where quantum computational approaches may have a significant impact in understanding and developing materials for technological applications.

## DATA AVAILABILITY

Data and code from this study are available online at <https://code.ornl.gov/5ci/dataset-simulations-of-frustrated-ising-hamiltonians-using-qaoa>

## AUTHOR CONTRIBUTIONS

P.C.L., A.B., and T.S.H. designed the experiments and analyzed the results. GB analyzed the results and provided feedback on the manuscript. P.C.L. composed the quantum programs and executed them in software and on hardware. H.X. performed the finite size analysis and helped with comparison of results with classical scenarios with the help from B.K. All authors contributed to writing and approved the presentation of these results.

## COMPETING INTERESTS

The authors declare that they have no competing interests.

## FUNDING

This material is based upon work supported by the U.S. Department of Energy, Office of Science, National Quantum Information Science Research Centers, Quantum Science Center.

## ACKNOWLEDGEMENTS

The authors thank Paul Kairys for interesting discussions. This research used resources of the Oak Ridge Leadership Computing Facility at the Oak Ridge National Laboratory, which is supported by the Office of Science of the U.S. Department of Energy under Contract No. DE-AC05-00OR22725. P.C.L. and T.S.H. acknowledge support from the Office of Science, Early Career Research Program. A.B., G.B. and B.K. acknowledge funding from the U.S. Department of Energy, Office of Science, National Quantum Information Science Research Centers, Quantum Science Center.

- 
- [1] Stephen John Blundell. *Magnetism in condensed matter*. Oxford University Press, 2014.
  - [2] H.Y. Yuan, Yunshan Cao, Akashdeep Kamra, Rembert A. Duine, and Peng Yan. Quantum magnonics: When magnon spintronics meets quantum information science. *Physics Reports*, 965:1–74, 2022.
  - [3] Roderich Moessner and Arthur P. Ramirez. Geometrical frustration. *Physics Today*, 59(2):24–29, 2006.
  - [4] A.P. Ramirez. Chapter 4 geometrical frustration. volume 13 of *Handbook of Magnetic Materials*, pages 423–520. Elsevier, 2001.
  - [5] A P Ramirez. Strongly geometrically frustrated magnets. *Annual Review of Materials Science*, 24(1):453–480, 1994.
  - [6] Oleg A Starykh. Unusual ordered phases of highly frustrated magnets: a review. *Reports on Progress in Physics*, 78(5):052502, apr 2015.
  - [7] Matthias Vojta. Frustration and quantum criticality. *Reports on Progress in Physics*, 81(6):064501, may 2018.
  - [8] C. Broholm, R. J. Cava, S. A. Kivelson, D. G. Nocera, M. R. Norman, and T. Senthil. Quantum spin liquids. *Science*, 367(6475), 2020.
  - [9] Antonio Ortiz-Ambriz, Cristiano Nisoli, Charles Reichhardt, Cynthia J. O. Reichhardt, and Pietro Tierno. Colloquium: Ice rule and emergent frustration in particle ice and beyond. *Rev. Mod. Phys.*, 91:041003, Dec 2019.
  - [10] Christian Wessler, Bertrand Roessli, Karl W. Krämer, Bernard Delley, Oliver Waldmann, Lukas Keller, Denis Cheptiakov, Hans B. Braun, and Michel Kennelmann. Observation of plaquette fluctuations in the spin-1/2 honeycomb lattice. *npj Quantum Materials*, 5(1), 2020.
  - [11] A. Banerjee, C. A. Bridges, J.-Q. Yan, A. A. Aczel, L. Li, M. B. Stone, G. E. Granroth, M. D. Lumsden, Y. Yiu, J. Knolle, and et al. Proximate Kitaev quantum spin liquid behaviour in a honeycomb magnet. *Nature Materials*, 15(7):733–740, 2016.
  - [12] Albert Fert, Nicolas Reyren, and Vincent Cros. Magnetic skyrmions: Advances in physics and potential applications. *Nature Reviews Materials*, 2(7), 2017.
  - [13] K. J. Satzinger, Y.-J Liu, A. Smith, C. Knapp, M. Newman, C. Jones, Z. Chen, C. Quintana, X. Mi, A. Dunsworth, and et al. Realizing topologically ordered states on a quantum processor. *Science*, 374(6572):1237–1241, 2021.
  - [14] Giuliano Giudici, Mikhail D. Lukin, and Hannes Pichler. Dynamical preparation of quantum spin liquids in Rydberg atom arrays. *arXiv:2201.04034*, 2022.
  - [15] A. M. Samarakoon, A. Banerjee, S.-S. Zhang, Y. Kamiya, S. E. Nagler, D. A. Tennant, S.-H. Lee, and C. D. Batista. Comprehensive study of the dynamics of a classical Kitaev spin liquid. *Physical Review B*, 96(13), 2017.
  - [16] Stephen M. Winter, Ying Li, Harald O. Jeschke, and Roser Valentí. Challenges in design of Kitaev materials: Magnetic interactions from competing energy scales. *Physical Review B*, 93(21), 2016.
  - [17] Qianke Zhu, Zhe Chen, Shuling Zhang, Qiushu Li, Yong Jiang, Peixuan Wu, and Kewei Zhang. Improving soft magnetic properties in FINEMET-like alloys with Ga addition. *Journal of Magnetism and Magnetic Materials*, 487:165297, 2019.
  - [18] Aaron Szasz, Johannes Motruk, Michael P. Zaletel, and Joel E. Moore. Chiral spin liquid phase of the triangular lattice Hubbard model: A density matrix renormalization group study. *Physical Review X*, 10(2), 2020.
  - [19] E.M. Stoudenmire and Steven R. White. Studying two-dimensional systems with the density matrix renormalization group. *Annual Review of Condensed Matter Physics*, 3(1):111–128, 2012.
  - [20] Stefan Wessel, B. Normand, Frédéric Mila, and Andreas Honecker. Efficient Quantum Monte Carlo simulations of highly frustrated magnets: the frustrated spin-1/2 ladder. *SciPost Phys.*, 3:005, 2017.
  - [21] Yoshitomo Kamiya, Yasuyuki Kato, Joji Nasu, and Yukitoshi Motome. Magnetic three states of matter: A quantum Monte Carlo study of spin liquids. *Physical Review B*, 92(10), 2015.
  - [22] Matthias Troyer and Uwe-Jens Wiese. Computational complexity and fundamental limitations to fermionic quantum Monte Carlo simulations. *Phys. Rev. Lett.*, 94:170201, May 2005.
  - [23] Anjana M. Samarakoon, Pontus Laurell, Christian Balz, Arnab Banerjee, Paula Lampen-Kelley, David Mandrus, Stephen E. Nagler, Satoshi Okamoto, and D. Alan Tennant. Extraction of the interaction parameters for  $\alpha$ -RuCl<sub>3</sub> from neutron data using machine learning, 2022.
  - [24] Zhenyue Zhu, P. A. Maksimov, Steven R. White, and A. L. Chernyshev. Disorder-induced mimicry of a spin liquid in YbMgGaO<sub>4</sub>. *Phys. Rev. Lett.*, 119:157201, Oct 2017.
  - [25] Ehud Altman, Kenneth R. Brown, Giuseppe Carleo, Lincoln D. Carr, Eugene Demler, Cheng Chin, Brian DeMarco, Sophia E. Economou, Mark A. Eriksson, Kai-Mei C. Fu, Markus Greiner, Kaden R.A. Hazzard, Randall G. Hulet, Alicia J. Kollár, Benjamin L. Lev, Mikhail D. Lukin, Ruichao Ma, Xiao Mi, Shashank Misra, Christopher Monroe, Kater Murch,

- Zaira Nazario, Kang-Kuen Ni, Andrew C. Potter, Pedram Roushan, Mark Saffman, Monika Schleier-Smith, Irfan Siddiqi, Raymond Simmonds, Meenakshi Singh, I.B. Spielman, Kristan Temme, David S. Weiss, Jelena Vučković, Vladan Vuletić, Jun Ye, and Martin Zwierlein. Quantum simulators: Architectures and opportunities. *PRX Quantum*, 2:017003, Feb 2021.
- [26] I. M. Georgescu, S. Ashhab, and Franco Nori. Quantum simulation. *Rev. Mod. Phys.*, 86:153–185, Mar 2014.
- [27] Andrew D. King, Cristiano Nisoli, Edward D. Dahl, Gabriel Poulin-Lamarre, and Alejandro Lopez-Bezanilla. Qubit spin ice. *Science*, 373(6554):576–580, 2021.
- [28] R. Harris, Y. Sato, A. J. Berkley, M. Reis, F. Altomare, M. H. Amin, K. Boothby, P. Bunyk, C. Deng, C. Enderud, and et al. Phase transitions in a programmable quantum spin glass simulator. *Science*, 361(6398):162–165, 2018.
- [29] Dolev Bluvstein, Harry Levine, Giulia Semeghini, Tout T. Wang, Sepehr Ebadi, Marcin Kalinowski, Alexander Keesling, Nishad Maskara, Hannes Pichler, Markus Greiner, and et al. A quantum processor based on coherent transport of entangled atom arrays. *Nature*, 604(7906):451–456, 2022.
- [30] Edward Farhi, Jeffrey Goldstone, and Sam Gutmann. A quantum approximate optimization algorithm. *arXiv:1411.4028*, 2014.
- [31] Andrew Lucas. Ising formulations of many NP problems. *Front. Phys.*, 2, 2014.
- [32] Yu. I. Dublenych. Ground states of the Ising model on the Shastry-Sutherland lattice and the origin of the fractional magnetization plateaus in rare-earth-metal tetraborides. *Phys. Rev. Lett.*, 109:167202, Oct 2012.
- [33] W C Huang, L Huo, G Tian, H R Qian, X S Gao, M H Qin, and J-M Liu. Multi-step magnetization of the Ising model on a Shastry-Sutherland lattice: a Monte Carlo simulation. *Journal of Physics: Condensed Matter*, 24(38):386003, aug 2012.
- [34] Paul Kairys, Andrew D. King, Isil Ozfidan, Kelly Boothby, Jack Raymond, Arnab Banerjee, and Travis S. Humble. Simulating the Shastry-Sutherland Ising model using quantum annealing. *PRX Quantum*, 1:020320, Dec 2020.
- [35] Akshat A. Jha, Eliana L. Stoyanoff, Guga Khundzakishvili, Paul Kairys, Hayato Ushijima-Mwesigwa, and Arnab Banerjee. Digital annealing route to complex magnetic phase discovery. *2021 International Conference on Rebooting Computing (ICRC)*, 2021.
- [36] Pavol Farkašovský, Hana Čenčariková, and Slavomír Mat’áš. Numerical study of magnetization processes in rare-earth tetraborides. *Phys. Rev. B*, 82:054409, Aug 2010.
- [37] Jennifer Trinh, Sreemanta Mitra, Christos Panagopoulos, Tai Kong, Paul C. Canfield, and Arthur P. Ramirez. Degeneracy of the 1/8 plateau and antiferromagnetic phases in the Shastry-Sutherland magnet  $\text{TmB}_4$ . *Phys. Rev. Lett.*, 121:167203, Oct 2018.
- [38] K. Siemensmeyer, E. Wulf, H.-J. Mikeska, K. Flachbart, S. Gabáni, S. Mat’áš, P. Priputen, A. Efdokimova, and N. Shitsevalova. Fractional magnetization plateaus and magnetic order in the Shastry-Sutherland magnet  $\text{TmB}_4$ . *Phys. Rev. Lett.*, 101:177201, Oct 2008.
- [39] Linda Ye, Takehito Suzuki, and Joseph G. Checkelsky. Electronic transport on the Shastry-Sutherland lattice in Ising-type rare-earth tetraborides. *Phys. Rev. B*, 95:174405, May 2017.
- [40] A. S. Panfilov, G. E. Grechnev, I. P. Zhuravleva, A. V. Fedorchenko, and V. B. Muratov. Specific features of the magnetic properties of  $\text{RB}_4$  ( $R = \text{Ce}, \text{Sm}$  and  $\text{Yb}$ ) tetraborides. effects of pressure. *Low Temperature Physics*, 41(3):193–198, 2015.
- [41] J. Y. Kim, N. H. Sung, B. Y. Kang, M. S. Kim, B. K. Cho, and Jong-Soo Rhyee. Magnetic anisotropy and magnon gap state of  $\text{SmB}_4$  single crystal. *Journal of Applied Physics*, 107(9), 2010.
- [42] S. Yoshii, K. Ohoyama, K. Kurosawa, H. Nojiri, M. Matsuda, P. Frings, F. Duc, B. Vignolle, G. L. J. A. Rikken, L.-P. Regnault, S. Michimura, and F. Iga. Neutron diffraction study on the multiple magnetization plateaus in  $\text{TbB}_4$  under pulsed high magnetic field. *Phys. Rev. Lett.*, 103:077203, Aug 2009.
- [43] Yair Shokef, Anton Souslov, and T. C. Lubensky. Order by disorder in the antiferromagnetic Ising model on an elastic triangular lattice. *Proceedings of the National Academy of Sciences*, 108(29):11804–11809, 2011.
- [44] Yu I Dublenych. Ground states of the Ising model on an anisotropic triangular lattice: stripes and zigzags. *Journal of Physics: Condensed Matter*, 25(40):406003, sep 2013.
- [45] F Barahona. On the computational complexity of Ising spin glass models. *Journal of Physics A: Mathematical and General*, 15(10):3241–3253, 1982.
- [46] Alain Billionnet and Sourour Elloumi. Using a mixed integer quadratic programming solver for the unconstrained quadratic 0-1 problem. *Mathematical Programming*, 109(1):55–68, 2006.
- [47] S. Kirkpatrick, C. D. Gelatt, and M. P. Vecchi. Optimization by simulated annealing. *Science*, 220(4598):671–680, 1983.
- [48] Alex Selby. Efficient subgraph-based sampling of Ising-type models with frustration, 2014.
- [49] Andrew D. King, Juan Carrasquilla, Jack Raymond, Isil Ozfidan, Evgeny Andriyash, Andrew Berkley, Mauricio Reis, Trevor Lanting, Richard Harris, Fabio Altomare, and et al. Observation of topological phenomena in a programmable lattice of 1,800 qubits. *Nature*, 560(7719):456–460, 2018.
- [50] G. Semeghini, H. Levine, A. Keesling, S. Ebadi, T. T. Wang, D. Bluvstein, R. Verresen, H. Pichler, M. Kalinowski, R. Samajdar, and et al. Probing topological spin liquids on a programmable quantum simulator. *Science*, 374(6572):1242–1247, 2021.
- [51] D-Wave Systems. *dwave-neal*. <https://github.com/dwavesystems/dwave-neal>.
- [52] John Preskill. Quantum Computing in the NISQ era and beyond. *Quantum*, 2:79, August 2018.
- [53] Phillip C. Lotshaw, Travis S. Humble, Rebekah Herrman, James Ostrowski, and George Siopsis. Empirical performance bounds for quantum approximate optimization. *Quant. Inf. Process.*, 20:403, 2021.
- [54] Leo Zhou, Sheng-Tao Wang, Soonwon Choi, Hannes Pichler, and Mikhail D. Lukin. Quantum approximate optimization algorithm: performance, mechanism, and implementation on near-term devices. *Phys. Rev. X*, 10:021067, 2020.
- [55] Jeremy Cook, Stephan Eidenbenz, and Andreas Bartschi. The quantum alternating operator ansatz on maximum  $k$ -vertex cover. *arXiv:1910.13483v2*, 2020.

- [56] Pontus Vikstål, Mattias Grönkvist, Marika Svensson, Martin Andersson, Göran Johansson, and Giulia Ferrini. Applying the quantum approximate optimization algorithm to the tail-assignment problem. *Phys. Rev. Applied*, 14:034009, Sep 2020.
- [57] Stuart Harwood, Claudio Gambella, Dimitar Tenev, Andrea Simonetto, David Bernal, and Donny Greenberg. Formulating and solving routing problems on quantum computers. *IEEE Transactions on Quantum Engineering*, 2, 2021.
- [58] Stuart Hadfield, Zhihui Wang, Bryan O’Gorman, Eleanor G Rieffel, Davide Venturelli, and Rupak Biswas. From the quantum approximate optimization algorithm to a quantum alternating operator ansatz. *Algorithms*, 12(2):34, 2019.
- [59] Taylor L. Patti, Jean Kossaifi, Anima Anandkumar, and Susanne F. Yelin. Nonlinear quantum optimization algorithms via efficient Ising model encodings. *arXiv:2106.13304*, 2021.
- [60] R. Herrman, P. C. Lotshaw, J. Ostrowski, T. S. Humble, and G. Siopsis. Multi-angle quantum approximate optimization algorithm. *arXiv preprint arXiv:2109.11455*, 2021.
- [61] Edward Farhi, Jeffrey Goldstone, Sam Gutmann, and Hartmut Neven. Quantum algorithms for fixed qubit architectures. *arXiv preprint arXiv:1703.06199*, 2017.
- [62] Reuben Tate, Majid Farhadi, Creston Herold, Greg Mohler, and Swati Gupta. Bridging classical and quantum with SDP initialized warm-starts for QAOA. *arXiv:2010.14021*, 2020.
- [63] Linghua Zhu, Ho Lun Tang, George S. Barron, Nicholas J. Mayhall, Edwin Barnes, and Sophia E. Economou. An adaptive quantum approximate optimization algorithm for solving combinatorial problems on a quantum computer. *arXiv:2005.10258*, 2020.
- [64] Vladimir Kremenetski, Tad Hogg, Stuart Hadfield, Stephen J. Cotton, and Norm M. Tubman. Quantum alternating operator ansatz (QAOA) phase diagrams and applications for quantum chemistry. *arXiv:2108.13056v2*, 2021.
- [65] Wen Wei Ho and Timothy H. Hsieh. Efficient variational simulation of non-trivial quantum states. *SciPost Phys.*, 6:029, 2019.
- [66] Gabriel Matos, Sonika Johri, and Zlatko Papić. Quantifying the efficiency of state preparation via quantum variational eigensolvers. *Phys. Rev. X Quantum*, 2:010309, 2021.
- [67] Guido Pagano, Aniruddha Bapat, Patrick Becker, Katherine S Collins, Arinjoy De, Paul W Hess, Harvey B Kaplan, Antonis Kyprianidis, Wen Lin Tan, Christopher Baldwin, et al. Quantum approximate optimization of the long-range Ising model with a trapped-ion quantum simulator. *Proceedings of the National Academy of Sciences*, 117(41):25396–25401, 2020.
- [68] Panagiotis Kl. Barkoutsos, Giacomo Nannicini, Anton Robert, Ivano Tavernelli, and Stefan Woerner. Improving variational quantum optimization using CVaR. *Quantum*, 4:256, 2020.
- [69] Li Li, Minjie Fan, Marc Coram, Patrick Riley, and Stefan Leichenauer. Quantum optimization with a novel Gibbs objective function and ansatz architecture search. *Phys. Rev. Research*, 2, 2020.
- [70] Gavin E Crooks. Performance of the quantum approximate optimization algorithm on the maximum cut problem. *arXiv:1811.08419*, 2018.
- [71] Joao Basso, Edward Farhi, Kunal Marwaha, Benjamin Villalonga, and Leo Zhou. The quantum approximate optimization algorithm at high depth for MaxCut on large-girth regular graphs and the Sherrington-Kirkpatrick model. *arXiv:2110.14206*, 2022.
- [72] R. Shaydulin, P. C. Lotshaw, J. Larson, J. Ostrowski, and T. S. Humble. Parameter transfer for quantum approximate optimization of weighted MaxCut. *arXiv:2201.11785*, 2022.
- [73] Quantinuum. Quantinuum system model H1 product data sheet, March 31, 2022.
- [74] Quantinuum. Quantinuum system model H1 emulator product data sheet, March 31, 2022.
- [75] Tiffany M. Mintz, Alexander J. McCaskey, Eugene F. Dumitrescu, Shirley V. Moore, Sarah Powers, and Pavel Lougovski. QCOR: A language extension specification for the heterogeneous quantum-classical model of computation. *ACM Journal on Emerging Technologies in Computing Systems*, 16(22):1–17, 2020.
- [76] Heiko Rieger and A. Peter Young. Quantum spin glasses. In Miguel Rubí and Conrado Pérez-Vicente, editors, *Complex Behaviour of Glassy Systems*, pages 256–265, Berlin, Heidelberg, 1997. Springer Berlin Heidelberg.
- [77] Pascal Reiss, David Graf, Amir A. Haghighirad, Thomas Vojta, and Malaia I. Coldea. Signatures of a quantum Griffiths phase close to an electronic nematic quantum phase transition. *Phys. Rev. Lett.*, 127:246402, 2021.
- [78] Ze Hu, Zhen Ma, Yuan-Da Liao, Han Li, Chunsheng Ma, Yi Cui, Yanyan Shangguan, Zhentao Huang, Yang Qi, Wei Li, Zi Yang Meng, Jinsheng Wen, and Weiqiang Yu. Evidence of the Berezinskii-Kosterlitz-Thouless phase transition in a frustrated magnet. *Nat. Comm.*, 11:5631, 2020.
- [79] J. M. Kosterlitz and D. J. Thouless. Ordering, metastability and phase transitions in two-dimensional systems. *J. Phys. C: Solid State Physics*, 6:1181–1203, 1973.
- [80] L. D. C. Jaubert and P. C. W. Holdsworth. Signature of magnetic monopole and Dirac string dynamics in spin ice. *Nat. Phys.*, 5:258–261, 2009.

## Appendix A: Circuits for quantum computations

Circuits for quantum computations are implemented using a decomposition of the QAOA unitaries in (6) into one- and two-qubit gates that are implemented on the trapped-ion quantum computer. To devise these circuits we begin by separating commuting terms to express the QAOA unitary dynamics in terms of one- and two-qubit operations.



This is accomplished by noting that

$$e^{-i\beta_l B} = \prod_{i=1}^N e^{-i\beta_l X_i} \quad (\text{A1})$$

and

$$e^{-i\gamma_l H} = \left( \prod_{(i,j) \in \text{NN}} e^{-iJ_1 \gamma_l Z_i Z_j} \right) \left( \prod_{(i,j) \in \text{NNN}} e^{-iJ_2 \gamma_l Z_i Z_j} \right) \left( \prod_{i=1}^N e^{-ih\gamma_l Z_i} \right), \quad (\text{A2})$$

where each component operation on the right now acts on at most two-qubits.

To implement these operations on the quantum computer, we first map the operations to a set of gates containing controlled-NOT (CNOT), Hadamard (H), and  $Z$ -rotation gates  $R(\theta) = \exp(-i(\theta/2)Z)$ . In terms of these gates, the component unitary operations are

$$\begin{aligned} e^{-i\beta_l X_i} &= H_i R_i(2\beta_l) H_i, \\ e^{-iJ_1 \gamma_l Z_i Z_j} &= \text{CNOT}_{i,j} R_j(2J_1 \gamma_l) \text{CNOT}_{i,j}, \\ e^{-ih\gamma_l Z_i} &= R_i(2h\gamma_l). \end{aligned} \quad (\text{A3})$$

We use QCOR [75] to automatically apply these transformations to our component circuit operations in (A1)-(A2) and send the resulting circuits to Quantinuum to perform our QAOA quantum computations.

The Quantinuum backend maps the operations (A3) into hardware-native gates that are implemented on the quantum computer [73]. These hardware native gates are defined as

$$\begin{aligned} U^{(1)}(\theta, \varphi) &= e^{-i(\theta/2)(\cos(\varphi)X + \sin(\varphi)Y)}, \\ ZZ_{i,j} &= e^{-i(\pi/4)Z_i Z_j}, \end{aligned} \quad (\text{A4})$$

and a rotation gate  $R(\theta) = \exp(-i(\theta/2)Z)$  (the same as our earlier definition). The circuits are then implemented on hardware using [73]

$$\begin{aligned} H_i &= R_i(\pi) U_i^{(1)}(\pi/2, -\pi/2) \\ \text{CNOT}_{i,j} &= R_j(-\pi/2) U_j^{(1)}(\pi/2, \pi) R_i(-\pi/2) ZZ_{i,j} U_j^{(1)}(-\pi/2, \pi/2). \end{aligned} \quad (\text{A5})$$

## Appendix B: State preparation and measurement error analysis

To characterize the SPAM error that is expected in our quantum computations, we use the Honeywell emulator H1-1E described in Sec. III B. We ran two circuits to characterize the readout error. The first circuit is designed to test the error in reading out the  $|0\rangle$  state for each qubit. This is accomplished by measuring the initial states of the quantum computation, which are designed such that each qubit is in its  $|0\rangle$  state. The second circuit applies a Pauli  $X$  operator to each qubit before measurement, ideally preparing a state with each qubit is in the  $|1\rangle$  basis state. For each of these circuits, we ran 1000 shots to characterize the noise in state preparation and measurement.

The results in Table II show the measurement results we obtained. They mainly consist of single-qubit errors, while only two instances of two-qubit errors were observed, and no errors were observed on more than two qubits at a time. The probability to observe no error is about 96% for each circuit.

To mitigate the influence of these errors, we use a model with independent errors in each qubit such that  $1 \rightarrow 0$  or  $0 \rightarrow 1$  with probability  $\epsilon$  for each qubit. The probability of zero errors is then  $P_{\text{no error}} = (1 - \epsilon)^n$  where  $n = 9$  is the number of qubits. We set  $P_{\text{no error}} = 0.96$  based on the results in Table II. The single qubit error rate is then computed as  $\epsilon = 1 - 0.96^{1/9} = 0.0045$ . This is in line with the results in the Table, where approximately 4–5 single-qubit errors of each type are observed out of 1,000 measurements, with deviations attributable to finite sampling.

Using the model for measurement errors, we can try to reverse their effects in measurements we observe from the quantum computations. From our independent bit-flip model, we construct a matrix  $\tilde{P}$  that accounts for expected effects of measurement errors. The matrix elements of  $\tilde{P}$  are expressed as

$$\tilde{P}_{\mathbf{z}', \mathbf{z}} = P(\mathbf{z}' | \mathbf{z}) = \epsilon^{\text{Ham}(\mathbf{z}', \mathbf{z})} (1 - \epsilon)^{n - \text{Ham}(\mathbf{z}', \mathbf{z})} \quad (\text{B1})$$

prepared state	no error	$q_1$	$q_2$	$q_3$	$q_4$	$q_5$	$q_6$	$q_7$	$q_8$	$q_9$
000000000	953	0	6	9	6	3	2	6	6	7
111111111	965	5	4	5	6	1	5	1	4	4

TABLE II: State preparation and measurement errors observed for circuits preparing the all-zero and all-one states. The columns  $q_x$  indicate a single qubit error in qubit number  $x$ , e.g. in row 000000000 the column  $q_2$  tells how many times 000000010 was observed (where there is an error in qubit 2). The all-zero state had two additional multi-qubit errors not listed in the table, with measured states 010100000 and 100010000.

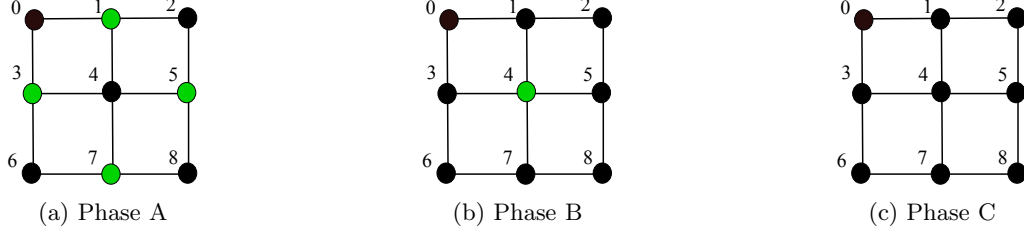


FIG. 12: Ground states for the square lattice, for the regions “A”, “B”, “C” in Fig. 2(d).

where  $P(\mathbf{z}'|\mathbf{z})$  is the probability to measure  $\mathbf{z}'$  conditional on the noiseless output being  $\mathbf{z}$  and  $\text{Ham}(\mathbf{z}, \mathbf{z}')$  is the Hamming distance between  $\mathbf{z}$  and  $\mathbf{z}'$ . For a vector of measured probabilities  $\tilde{\mathbf{m}}$ , we can then attempt to correct the expected errors by computing the mitigated measurement vector as  $\mathbf{m} = \tilde{P}^{-1}\tilde{\mathbf{m}}$ . This is expected to approximately counteract the deleterious effects of SPAM errors.

The simple measurement mitigation model of the previous paragraph suffers from a non-physical deficiency: when the total number of measurements is small, then sampling introduces randomness into the observed  $\tilde{\mathbf{m}}$  and attempts to correct its errors with  $\tilde{P}^{-1}$  can lead to negative probabilities in the corrected counts  $\mathbf{m}$ . To overcome this deficiency, we consider a second type of model for measurement error mitigation in which every entry of  $\mathbf{m}$  that is less than zero is set to zero, then the total probabilities in  $\mathbf{m}$  are renormalized. This yields a set of error-mitigated probabilities that is physically reasonable in the sense that each probability is greater than or equal to zero.

### Appendix C: Ferromagnetic ground state preparation

Here we rationalize the large success probabilities for the ferromagnetic ground state in (7), based on limiting behavior of QAOA when  $h \gg J_1$ . In this limit, the QAOA evolution under  $H$  is approximately

$$e^{-i\gamma H} = e^{-i\gamma_1 h \sum_{i=1}^N Z_i} e^{-i\gamma J_1 \sum_{(i,j) \in \text{NN}} Z_i Z_j} \approx e^{-i\gamma_1 h \sum_{i=1}^N Z_i} \quad (\text{C1})$$

The total evolution in (6) then factorizes into separate components for each qubit, with single-qubit evolution  $\exp(-i\beta X_i) \exp(-i\gamma h Z_i)$ . The initial state for each qubit is  $|+\rangle = 2^{-1/2}(|0\rangle + |1\rangle)$ . For  $\gamma_1 h = \pi/4$ , the first step in the evolution yields  $\exp(-i\gamma_1 h Z_i)|+\rangle = 2^{-1/2}(|0\rangle + i|1\rangle)$ , up to a global phase which is not physically relevant. This corresponds to rotation on the Bloch sphere that takes the initial  $X$  eigenstate  $|+\rangle$  into a  $Y$  eigenstate  $|+i\rangle$ . For  $\beta = -\pi/4$ , the second operator  $\exp(-i\beta X_i)$  then generates the state  $|1\rangle$  up to a global phase. As these operators act separately on each qubit, there is no entanglement and the final state is  $|1\rangle^{\otimes n}$ , which is the ferromagnetic ground state.

### Appendix D: Ground States for Each Phase

Figures 12-14 visually depict the ground states observed at different values of the Hamiltonian parameters  $h/J_1$  and  $J_2/J_1$  for each phase of the square and Shastry-Sutherland lattices.

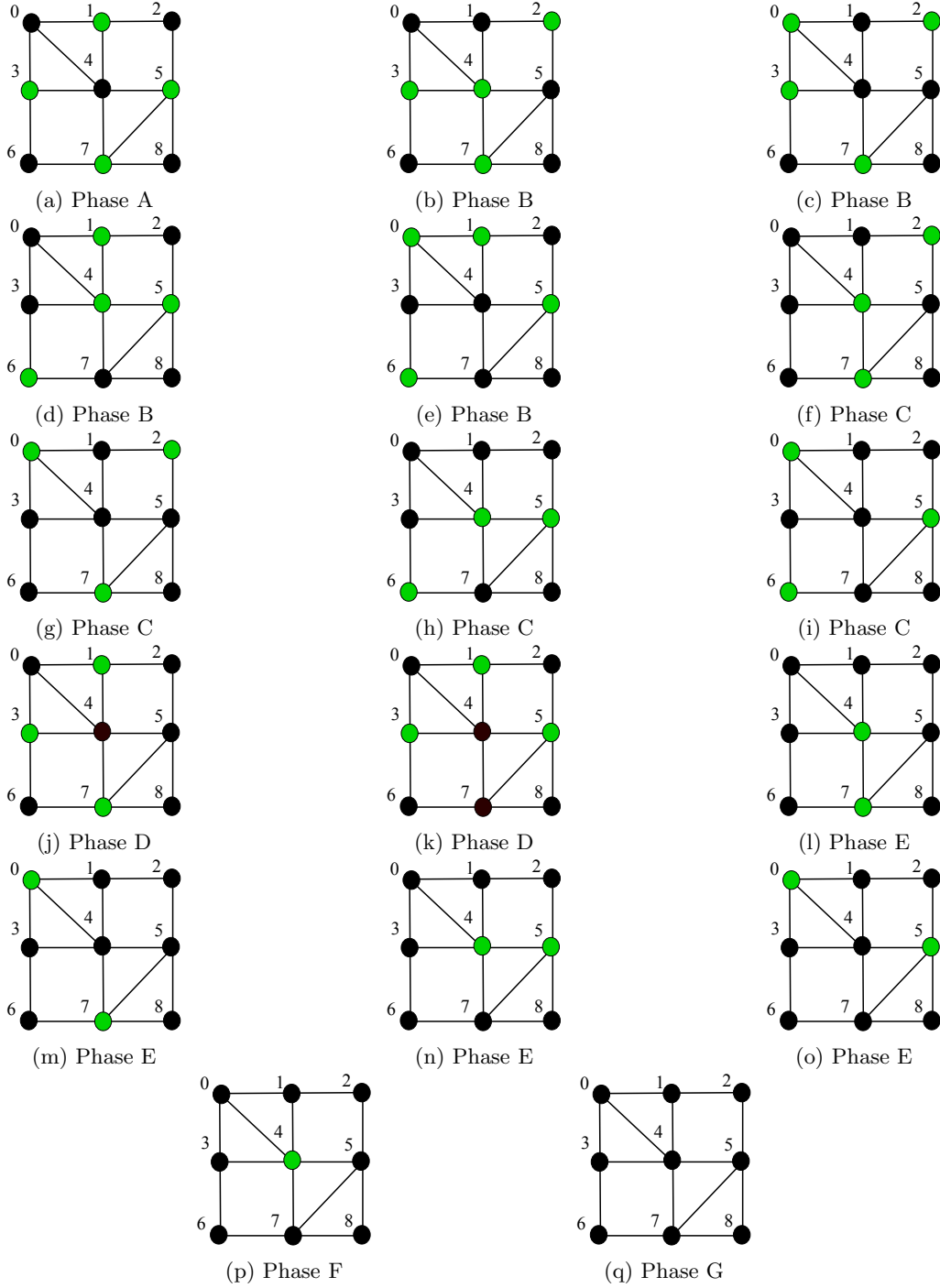


FIG. 13: Ground states for the square lattice, for the regions “A”, “B”, ... in Fig. 2(e).

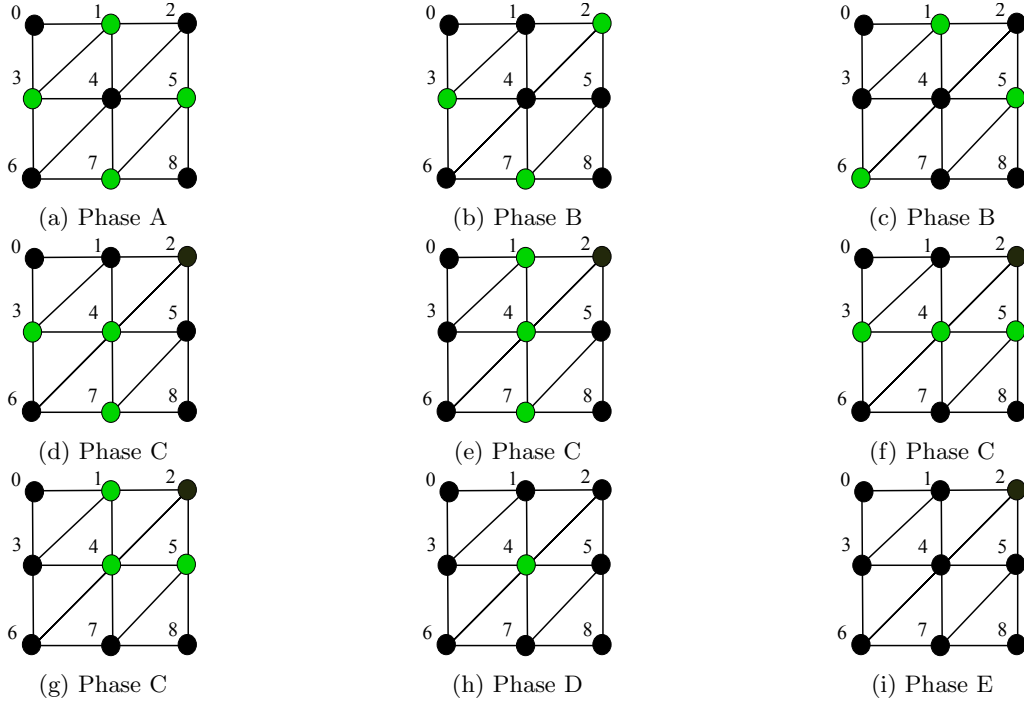


FIG. 14: Ground states for the triangular lattice, for the regions “A”, “B”, ... in Fig. 2(f).